times the rated torque. Motors can run smoothly at extremely low speeds, even when powered by a standard solid state converter. In addition, the high peak torque capability can allow, in certain applications, the elimination of costly gearboxes and reduce the risk of lubricant leaks.

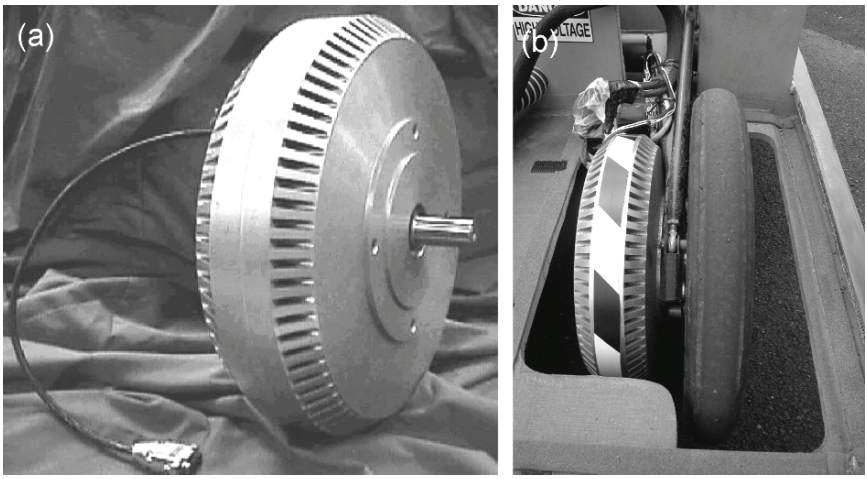


Fig. 5.1. AFPM brushless *e-TORQ*$^{\text{TM}}$ motor with coreless stator windings: (a) general view; (b) motor integrated with wheel of a solar powered car. Photo courtesy of *Bodine Electric Company*, Chicago, IL, U.S.A.

The 356-mm diameter *e-TORQ*$^{\text{TM}}$ motors have been used successfully by students of North Dakota State University for direct propulsion of a *solar powered car* participating in 2003 American Solar Challenge (Fig. 5.1b). A well designed solar-powered vehicle needs a very efficient and very light electric motor to convert the maximum amount of solar energy into mechanical energy at minimum rolling resistance. Coreless AFPM brushless motors satisfy these requirements.

Small ironless motors may have *printed circuit stator windings* or *film coil windings*. The film coil stator winding has many coil layers while the printed circuit winding has one or two coil layers. Fig. 5.2 shows an ironless brushless motor with film coil stator winding manufactured by *EmBest*, Soeul, South Korea. This motor has single-sided PM excitation system at one side of the stator and backing steel disc at the other side of the stator. Small film coil motors can be used in computer peripherals, computer hard disc drives (HDDs) [139, 140], mobile phones, pagers, flight recorders, card readers, copiers, printers, plotters, micrometers, labeling machines, video recorders and medical equipment.

Hesai Exhibit 1032, page 161

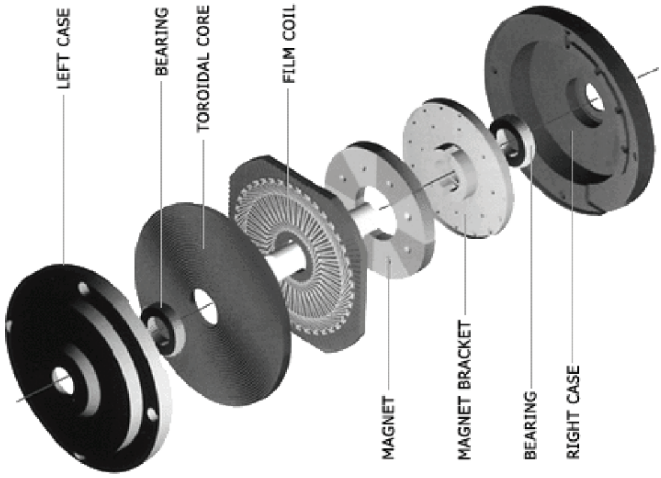


Fig. 5.2. Exploded view of the AFPM brushless motor with film coil coreless stator winding and single-sided rotor PM excitation system. Courtesy of *Embest*, Soeul, South Korea.

5.3 Coreless Stator AFPM Microgenerators

Fig. 5.3 shows an AFPM microgenerator developed at Georgia Institute of Technology, Atlanta, GA, U.S.A. [12, 13]. The stator uses interleaved, electroplated copper windings that are dielectrically isolated from a 1-mm thick NiFeMo substrate by a 5 μm polyimide layer. The rotor consists of a 2 to 12 pole, 500 μm thick, annular PM (OD = 10 mm, ID = 5 mm) and a 500 μm thick Hiperco 50 (FeCoV alloy) ring as a return path for the magnetic flux. SmCo PMs and Hiperco alloy have been used because microgenerators will be operating in high temperature environment, i.e., powered by gas-fueled turbine engines. Specifications are given in Table 5.1 [12].

A 16 W of mechanical–to–electrical power conversion and delivery of 8 W of d.c. power to a resistive load at a rotational speed of 305 krpm has been demonstrated [12]. The power density of the AFPM microgenerator was 59 W/cm^3.

5.4 Performance Calculation

5.4.1 Steady-State Performance

To calculate the steady-state performance of a coreless stator AFPM brushless machine it is essential to consider the equivalent circuits.

The *steady-state per phase equivalent circuit* of a coreless stator AFPM brushless machine may be represented by the circuit shown in Fig. 5.5, where

Hesai Exhibit 1032, page 162



Fig. 5.3. Experimental tests on AFPM microgenerators by spinning a small magnet with the aid of air-powered drill above a mesh of coils fabricated on a chip. Photo courtesy of Georgia Institute of Technology, Atlanta, GA, U.S.A.

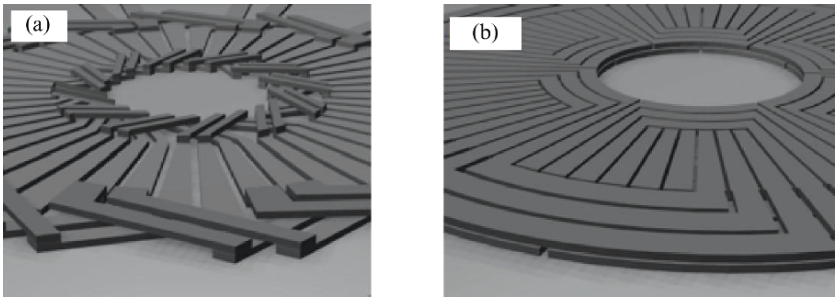


Fig. 5.4. Stator winding patterns for 8-pole microgenerator: (a) 2 turns per pole; (b) 3-turns pole. Photo courtesy of Georgia Institute of Technology, Atlanta, GA, U.S.A.

R_1 is the stator resistance, X_1 is the stator leakage reactance, E_f is the EMF induced in the stator winding by the rotor PM excitation system, E_i is the *rms* value of the internal phase voltage, V_1 is the terminal voltage and I_a is the *rms* stator current. The shunt resistance R_e is the stator eddy current loss resistance, which is defined in the same way as the core loss resistance [126] for slotted PM brushless motors.

The stator currents I_{ad}, I_{aq} and I_a for a given load angle δ (corresponding to the slip s in induction machines) can be calculated on the basis of eqns (2.87), (2.88) and (2.89) respectively. If $I_{ad} = 0$, all the stator current $I_a = I_{aq}$

Hesai Exhibit 1032, page 163

Table 5.1. Specifications of AFPM microgenerator fabricated at the School of Electrical and Computer Engineering, Georgia Institute of Technology, Atlanta, GA, U.S.A.

Number of poles	2 to 12
Number of turns per pole	1 to 6
Outer end turn extension	0 to 2.5 mm
Inner end turn extension	0 to 2.5 mm
Magnet outer radius, mm	5.0
Magnet inner radius, mm	2.5
Stator radial conductor outer radius, mm	4.75
Stator radial conductor inner radius, mm	2.75
Hiperco ring thickness, μm	500
Magnet thickness, μm	500
Radial conductor thickness, μm	200
End turn thickness, μm	80
Substrate thickness, μm	1000
Air gap, μm	100
Power electronics equivalent resistance, mΩ	100

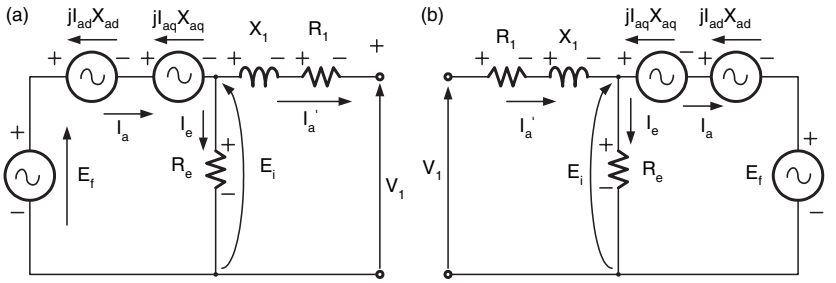


Fig. 5.5. Per phase equivalent circuit of an AFPM machine with a coreless stator: (a) generator arrow system; (b) consumer (motor) arrow system. Eddy current losses are accounted for by the shunt resistance R_e.

produces the electromagnetic torque and the load angle $\delta = \phi$. The angle ϕ between the stator current I_a and terminal voltage V_1 is determined by the power factor $\cos\phi$.

If we ignore the losses in PMs and losses in rotor backing steel discs, the input power can then be calculated as follows

- for the motoring mode (electrical power)

$$P_{in} = P_{elm} + \Delta P_{1w} + \Delta P_e \tag{5.1}$$

- for the generating mode (mechanical shaft power)

$$P_{in} = P_{elm} + \Delta P_{rot} \tag{5.2}$$

Hesai Exhibit 1032, page 164

where P_{elm} is the electromagnetic power according to eqn (2.91) in which $\Delta P_{1Fe} = 0$, ΔP_{1w} is the stator winding loss according to eqn (2.49), ΔP_e are the eddy current losses in the stator conductors according to eqn (2.68) or eqn (2.69) and ΔP_{rot} are the rotational losses according to eqn (2.70).

Similarly, the output power is:

- for the motoring mode (shaft power)

$$P_{out} = P_{elm} - \Delta P_{rot} \tag{5.3}$$

- for the generating mode (electrical power)

$$P_{out} = P_{elm} - \Delta P_{1w} - \Delta P_e \tag{5.4}$$

The shaft torque is given by eqn (4.30) for motoring mode or eqn (4.31) for generating mode, and the efficiency is expressed by eqn (4.32).

5.4.2 Dynamic Performance

For a salient pole synchronous machine without any rotor winding the voltage equations for the stator circuit are

$$v_{1d} = R_1 i_{ad} + \frac{d\psi_d}{dt} - \omega\psi_q \tag{5.5}$$

$$v_{1q} = R_1 i_{aq} + \frac{d\psi_q}{dt} + \omega\psi_d \tag{5.6}$$

in which the linkage fluxes are defined as

$$\psi_d = (L_{ad} + L_1) i_{ad} + \psi_f = L_{sd} i_{ad} + \psi_f \tag{5.7}$$

$$\psi_q = (L_{aq} + L_1) i_{aq} = L_{sq} i_{aq} \tag{5.8}$$

In the above equations (5.5) to (5.8) v_{1d} and v_{1q} are d- and q-axis components of the terminal voltage, ψ_f is the maximum flux linkage per phase produced by the excitation system, R_1 is the armature winding resistance, L_{ad}, L_{aq} are the d- and q-axis components of the armature self-inductance, $\omega = 2\pi f$ is the angular frequency of the armature current, i_{ad}, i_{aq} are the d- and q-axis components of the armature current. The resultant armature inductances $L_{sd} = L_{ad} + L_1$ and $L_{sq} = L_{aq} + L_1$ are referred to as synchronous inductances. In a three-phase machine $L_{ad} = (3/2)L'_{ad}$ and $L_{aq} = (3/2)L'_{aq}$ where L'_{ad} and L'_{aq} are self-inductances of a single phase machine. The excitation linkage flux $\psi_f = L_{fd} I_f$ where L_{fd} is the maximum value of the mutual inductance between the armature and field winding. In the case of a PM excitation, the fictitious field current is $I_f = H_c h_M$.

Putting eqns (5.7) and (5.8) into eqns (5.5) and (5.6), the stator voltage equations in the d and q-axis can be written as

Hesai Exhibit 1032, page 165

$$v_{1d} = R_1 i_{ad} + \frac{di_{ad}}{dt} L_{sd} - \omega L_{sq} i_{aq} \tag{5.9}$$

$$v_{1q} = R_1 i_{aq} + \frac{di_{aq}}{dt} L_{sq} + \omega L_{sd} i_{ad} + \omega \psi_f \tag{5.10}$$

For the steady state operation $(d/dt)L_{sd}i_{ad} = (d/dt)L_{sq}i_{aq} = 0$, $\mathbf{I}_a = I_{ad} + jI_{aq}$, $\mathbf{V}_1 = V_{1d} + jV_{1q}$, $i_{ad} = \sqrt{2}I_{ad}$, $i_{aq} = \sqrt{2}I_{aq}$, $v_{1d} = \sqrt{2}V_{1d}$, $v_{1q} = \sqrt{2}V_{1q}$, $E_f = \omega L_{fd} I_f/\sqrt{2} = \omega\psi_f/\sqrt{2}$ [94]. The quantities ωL_{sd} and ωL_{sq} are known as the $d-$ and q-axis synchronous reactances respectively.

The instantaneous power to the motor input terminals is [94, 106]

$$p_{in} = \frac{m_1}{2}(v_{1d} i_{ad} + v_{1q} i_{aq}) \tag{5.11}$$

The input power of a motor (5.11) is equivalent to the output power of a generator. The electromagnetic power of a three-phase machine is [94, 106]

$$p_{elm} = \frac{3}{2}\omega[\psi_f + (L_{sd} - L_{sq})i_{ad}]i_{aq} \tag{5.12}$$

The electromagnetic torque of a three phase motor with p pole pairs is

$$T_d = p\frac{p_{elm}}{\omega} = \frac{3}{2}p[\psi_f + (L_{sd} - L_{sq})i_{ad}]i_{aq} \tag{5.13}$$

The relationships between i_{ad}, i_{aq} and phase currents i_{aA}, i_{aB} and i_{aC} are

$$i_{ad} = \frac{2}{3}\left[i_{aA}\cos\omega t + i_{aB}\cos\left(\omega t - \frac{2\pi}{3}\right) + i_{aC}\cos\left(\omega t + \frac{2\pi}{3}\right)\right] \tag{5.14}$$

$$i_{aq} = -\frac{2}{3}\left[i_{aA}\sin\omega t + i_{aB}\sin\left(\omega t - \frac{2\pi}{3}\right) + i_{aC}\sin\left(\omega t + \frac{2\pi}{3}\right)\right] \tag{5.15}$$

The reverse relations, obtained by simultaneous solution of eqns (5.14) and (5.15) in conjunction with $i_{aA} + i_{aB} + i_{aC} = 0$, are

$$i_{aA} = i_{ad}\cos\omega t - i_{aq}\sin\omega t$$

$$i_{aB} = i_{ad}\cos\left(\omega t - \frac{2\pi}{3}\right) - i_{aq}\sin\left(\omega t - \frac{2\pi}{3}\right) \tag{5.16}$$

$$i_{aC} = i_{ad}\cos\left(\omega t + \frac{2\pi}{3}\right) - i_{aq}\sin\left(\omega t + \frac{2\pi}{3}\right)$$

Hesai Exhibit 1032, page 166

5.5 Calculation of Coreless Winding Inductances

5.5.1 Classical Approach

The synchronous inductance L_s consists of the armature reaction (mutual) inductance L_a and the leakage inductance L_1. For a machine with magnetic asymmetry, i.e. with a difference in reluctances in the d and q axes, the synchronous inductances in the $d-$ and q-axis, L_{sd} and L_{sq}, are written as sums of the armature reaction inductances (mutual inductances), L_{ad} and L_{aq}, and leakage inductance L_1, i.e.

$$L_{sd} = L_{ad} + L_1 \qquad L_{sq} = L_{aq} + L_1 \tag{5.17}$$

The armature reaction inductances are expressed by eqns (2.116), (2.117) and (2.118), in which air gaps in the d- and q-axis are given by eqns (2.112) and (2.113). The armature reaction reactances are given by eqns (2.121) and (2.122). Table 2.1 compares armature reaction equations for cylindrical and disc-type machines.

The leakage inductance is expressed analytically as a sum of three components, i.e.

$$L_1 = L_{1s} + L_{1e} + L_{1d} = 2\mu_0 \frac{N_1^2 L_i}{p q_1} (\lambda_{1s} + \frac{l_{1e}}{L_i} \lambda_{1e} + \lambda_{1d}) \tag{5.18}$$

where $L_i = 0.5(D_{out} - D_{in})$ is the active length of a coil equal to the radial length l_M of the PM, q_1 is the number of coil sides per pole per phase (equivalent to the number of slots) according to eqn (2.2), $l_{1e} = 0.5(l_{1in} + l_{1out})$ is the average length of the single-sided end connection, L_{1s} and λ_{ls} are the inductance and specific permeance for the leakage flux about radial portions of conductors (corresponding to slot leakage in classical machines) respectively, L_{1e} and λ_{1e} are the inductance and specific permeance for the leakage flux about the end connections respectively, and L_{1d} and λ_{1d} are the inductance and specific permeance for differential leakage flux (due to higher space harmonics) respectively.

It is difficult to derive an accurate analytical expression for λ_{1s} for a coreless electrical machine. The specific permeances λ_{1s} and λ_{1e} can roughly be estimated from the following semi-analytical equation:

$$\lambda_{1s} \approx \lambda_{1e} \approx 0.3 q_1 \tag{5.19}$$

The specific permeance for the differential leakage flux can be found in a similar way as for an induction machine [121], using eqn (4.22) in which $k_{sat} \approx 1$ and $g' \approx 2[(g+0.5t_w)+h_M]$. The thickness of the stator winding is t_w and the distance from the stator disc surface to the PM active surface is g (mechanical clearance). It is not difficult to show that $L_{1d} = L_a \tau_{d1}$ [121].

Hesai Exhibit 1032, page 167

5.5.2 FEM Approach

Unlike conventional slotted AFPM machines, there is no clear definition for main and leakage inductances in a coreless or slotless machine as discussed in [14, 85, 133]. Using the 2D FEM analysis both mutual and leakage fluxes can be taken into account. The only remaining part is the end winding leakage flux.

With the 2D finite element solution the magnetic vector potential $\mathbf{A}$ has only a z component, i.e. $\mathbf{A} = A(x, y) \cdot \hat{a}_z$ where $\hat{a}_z$ is the unit vector in z direction (axial direction). The total stator flux of a phase winding ψ_{ABC} that excludes the end-winding flux leakage can be readily calculated by using Stokes theorem, i.e.

$$\psi_{ABC} = \int_s \mathbf{B} \cdot \mathbf{dS} = \int_s \boldsymbol{\nabla} \times \mathbf{A} \cdot \mathbf{dS} = \oint_c \mathbf{A} \cdot \mathbf{dl} \tag{5.20}$$

As an approximation the flux linkage of a phase coil can be calculated by working out the difference between maximum magnetic vector potential values of each coil side. In the case that the coil is not very thin, magnetic vector potential varies in the coil cross-section area. Therefore, the average magnetic vector potential values should be used. For first-order triangular elements, the flux linkage of a coil with N_1 turns, area S and length l is given by [144]

$$\psi = N_1 \sum_{j=1}^{n} \frac{\Delta_j}{S} \left[\frac{\zeta}{3} \sum_{i=1}^{3} A_{ij} \right] l \tag{5.21}$$

where A_{ij} is the nodal value of the magnetic vector potential of the triangular element j, $\zeta = +1$ or $\zeta = -1$ indicates the direction of integration either into the plane or out of the plane, Δ_j is the area of the triangular element j, and n is the total number of elements of the in-going and out-going areas of the coil. It follows that for an AFPM machine with only one pole modelled, the total flux linkage of a phase winding is

$$\psi_{ABC} = \frac{2\ p\ N_1\ l}{a_p S} \sum_{j=1}^{u} \left[\frac{\Delta_j \zeta}{3} \sum_{i=1}^{3} A_{ij} \right] \tag{5.22}$$

where u is the total number of elements of the meshed coil areas of the phase in the pole region and a_p is the number of parallel circuits (parallel current paths) of the stator winding.

From a machine design perspective, it is important to find the fundamental components of the total flux linkages. For a coreless stator AFPM machine with usually unsaturated rotor yoke, the flux linkage harmonics due to iron stator slots and magnetic saturation are absent. Owing to the large air gap, the stator winding MMF space harmonics are negligible in most cases. The most

Hesai Exhibit 1032, page 168

important harmonics needed to account for are those due to the flat-shaped PMs.

Given these considerations, the flux linkage wave of an AFPM machine is nearly sinusoidal, though for a concentrated parameter (non-distributed) winding, an appreciable 3^{rd} and less significant 5^{th} and 7^{th} harmonics are still present in the total flux linkage waveform. If the 5^{th}, 7^{th} and higher harmonics are ignored, the fundamental total phase flux linkages can be calculated by using the technique given in [144], i.e.

$$[\psi_{ABC1}] \approx [\psi_{ABC}] - [\psi_{ABC3}] \tag{5.23}$$

where the co-phasal 3^{rd} harmonic flux linkage, including the higher order triple harmonics, can be obtained from:

$$\psi_{A3} = \psi_{A3} = \psi_{C3} \approx \frac{1}{3}(\psi_A + \psi_B + \psi_C) \tag{5.24}$$

With the fundamental total phase flux linkages and rotor position known, the d and q-axis flux linkages are calculated using Park's transformation as follows [94]:

$$[\psi_{dq0}] = [K_p]\,[\psi_{ABC1}] \tag{5.25}$$

where [94]

$$K_p = \frac{2}{3}\begin{bmatrix} \cos\theta & \cos(\theta - \frac{2\pi}{3}) & \cos(\theta + \frac{2\pi}{3}) \\ -\sin\theta & -\sin(\theta - \frac{2\pi}{3}) & -\sin(\theta + \frac{2\pi}{3}) \\ \frac{1}{2} & \frac{1}{2} & \frac{1}{2} \end{bmatrix} \tag{5.26}$$

With a constant rotor angular velocity ω the angle $\theta = \omega t$. In the 2D FEM model the d-axis and q-axis synchronous inductances do not include the component due to end connection leakage flux [106], i.e.

$$L'_{sd} = L_{ad} + L'_1 = L_{ad} + L_{1s} + L_{1d} \tag{5.27}$$

$$L'_{sq} = L_{aq} + L'_1 = L_{aq} + L_{1s} + L_{1d} \tag{5.28}$$

The inductances L'_{sd} and L'_{sq} result from eqns (5.7) and (5.8), i.e.

$$L'_{sd} = \frac{\psi_d - \psi_f}{i_{ad}} \quad \text{and} \quad L'_{sq} = \frac{\psi_q}{i_{aq}} \tag{5.29}$$

The end winding inductance L_{1e} can be calculated from numerical evaluation of the energy stored in the end connections [184] or simply by using an approximate equation resulting from eqn (5.18), i.e.

$$L_{1e} = 2\mu_0 \frac{N_1^2 l_{1e}}{p q_1} \lambda_{1e} \tag{5.30}$$

Finally,

Hesai Exhibit 1032, page 169

$$L_{sd} = L'_{sd} + L_{1e} \quad \text{and} \quad L_{sd} = L'_{sd} + L_{1e} \tag{5.31}$$

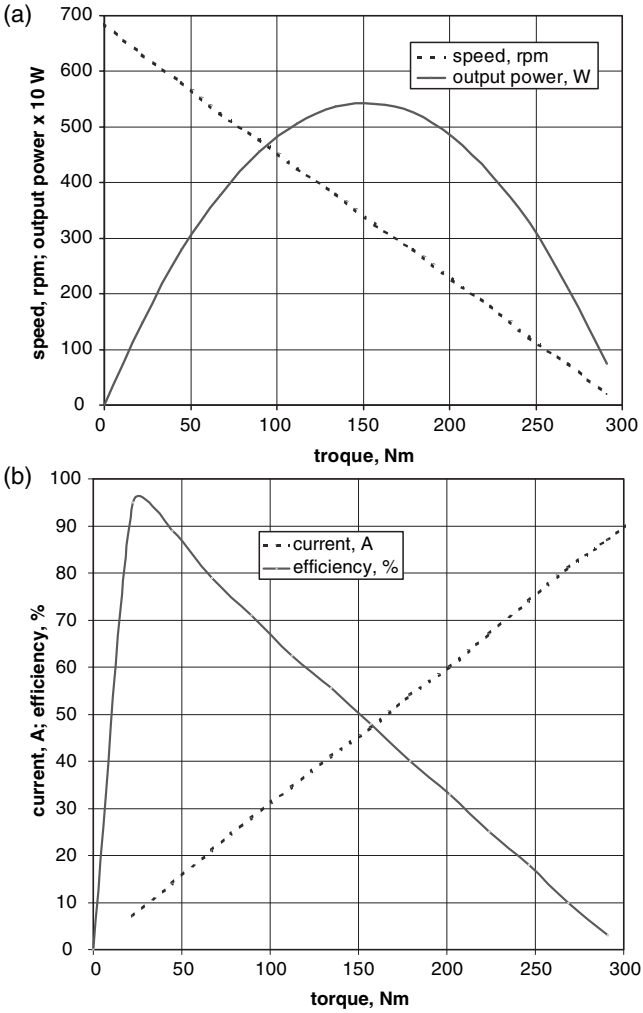


Fig. 5.6. Steady state characteristics of of 356-mm, 1-kW, 170-V *e-TORQ*™ AFPM motor: (a) output power P_{out} and speed n versus shaft torque T_{sh}; (b) phase current and efficiency versus shaft torque T_{sh}. Data captured at 22°C for totally enclosed non-ventilated motor. Courtesy of *Bodine Electric Company*, Chicago, IL, U.S.A.

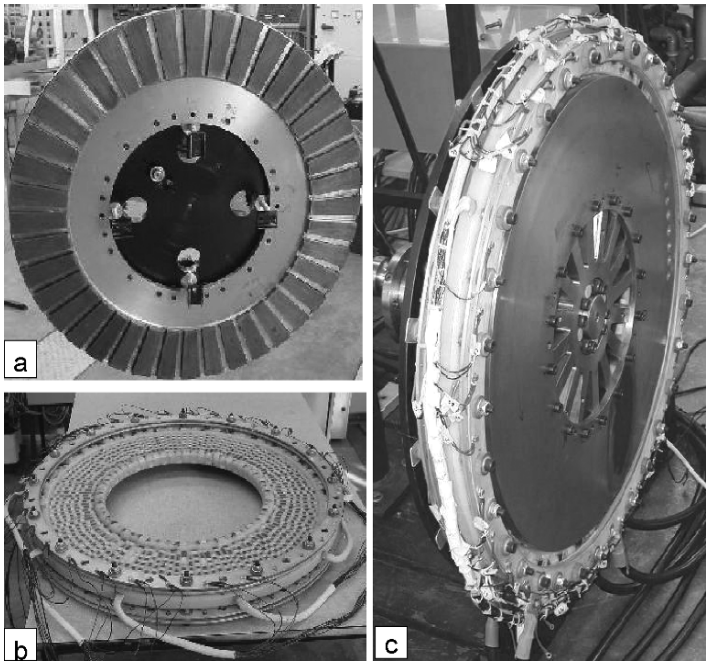


Fig. 5.7. Air-cooled single-stage synchronous AFPM machine: (a) rotor disc with surface mounted PM segments, (b) coreless stator with busbars, and (c) the assembled machine. Courtesy of the *University of Stellenbosch*, South Africa.

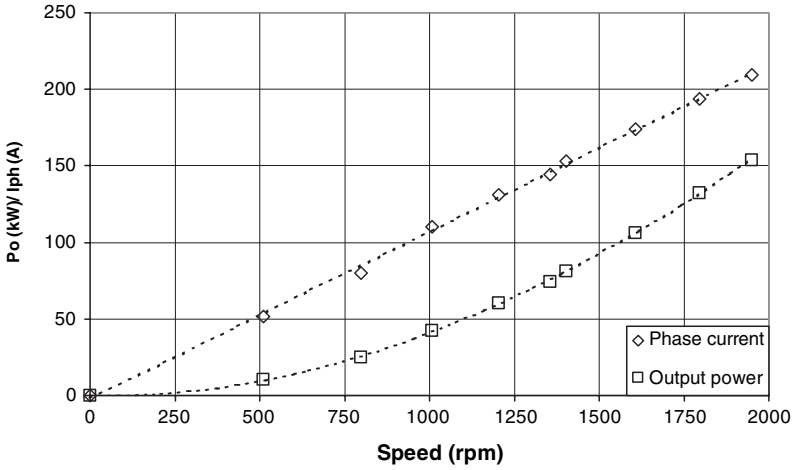


Fig. 5.8. Output power and phase current versus speed for generating mode of a 160-kW AFPM brushless generator. Specifications are given in Table 5.3.

Table 5.2. Specifications of *e-TORQ*^{TM} AFPM motors with coreless stators manufactured by *Bodine Electric Company*, Chicago, IL, U.S.A.

Parameter	178-mm AFPM motor		356-mm AFPM motor	
	Low EMF constant	High EMF constant	Low EMF constant	High EMF constant
Output power, kW	0.7	0.57	1.0	0.26
Number of poles	8	8	16	16
d.c. bus voltage, V	170	300	170	300
Speed, rpm	3000	1500	300	70
Peak speed, rpm	3500	2200	700	400
Torque, Nm	2.26	2.83	31.1	33.9
Peak torque, Nm	22.6	13.67	152.1	84.4
Current, A	5	2	13	5
Peak current, A	50	10.5	64	12.5
Efficiency, %	81	75	84	77
Torque constant, Nm/A	0.4859	1.299	2.38	6.814
EMF constant, V/krpm	50	137	249	713
Winding resistance, Ω	2.2	14.3	1.33	43
Winding inductance, mH	1.4	10.5	3.6	29.4
Viscous friction, Nm/rad/s	9.9×10^{-5}	0.00019	0.00669	0.012
Static friction, Nm	0.00728	0.0378	0.02357	0.1442
Electrical time constant, ms	0.6364	0.734	2.71	0.684
Mechanical time constant, ms	4.538	4.026	4.5	17.78
Moment of inertia, kgm^2	0.00525	0.00525	0.21	0.21
Mass of active parts, kg	6.17	6.17	30.87	30.87
Power density, W/kg	113.5	92.4	32.39	8.42

5.6 Performance Characteristics

Specifications of *e-TORQ*^{TM} AFPM brushless motors manufactured by *Bodine Electric Company*, Chicago, IL, U.S.A. are given in Table 5.2. The EMF constant, torque constant, winding resistance and winding inductance are line-to-line quantities. Motors are designed for a maximum winding continuous temperature of 130°C. Steady-state performance characteristics of a 356-mm, 1-kW, 170-V e-TORQ^{TM} motor are shown in Fig. 5.6.

Fig. 5.7 shows an air-cooled 160-kW AFPM brushless generator with a coreless stator built at the University of Stellenbosch, South Africa [260]. The stator winding consists of sixty single-layer trapezoidal-shape coils, which have the advantage of being easy to fabricate and have relatively short overhangs (Fig. 3.17). The winding coils are held together to form a disc-type stator by using composite material of epoxy resin and hardener. Sintered NdFeB PMs with $B_r \approx 1.16$ T and maximum allowable working temperature around 130°C have been used. The detailed design data are given in Table 5.3.

The output power and phase current at different speeds are shown in Fig. 5.8. Owing to very low stator winding inductance per phase, the output voltage varies almost linearly with the load current.

Hesai Exhibit 1032, page 172

Table 5.3. Specifications of a three-phase, 160-kW, 1950-rpm AFPM brushless synchronous generator with ironless stator core built at the *University of Stellenbosch*, South Africa

Design data	
Output power P_{out}, kW	160
Speed n, rpm	1950
Number of phases m_1	3 (Wye)
Rated line voltage, V	435
Rated phase current, A	215
Frequency f, Hz	100
Number of stator modules	1
Number of pole pairs p	20
Number of stator coils (3 phases)	60
Number of turns per phase	51
Wire diameter, mm	0.42
Number of parallel wires a_w	12
Axial height of PM per pole h_M, mm	10.7
Axial thickness of the winding t_w, mm	15.7
Air gap (one side) g, mm	2.75
Air gap magnetic flux density B_{mg} under load, T	0.58
Current density, A/mm^2	7.1
PM outer diameter D_{out}, mm	720
$k_d = D_{in}/D_{out}$ ratio	0.69
Class of insulation	F
Winding temperature rise, °C	56
Cooling system	Self air-cooled
Type of winding	Single layer trapezoidal

It has been found from both experimental tests and calculations that for a typical sine-wave AFPM machine with a coreless stator, the ratio of the d- and q-axis inductances of the phase winding is near unity, i.e. $L_{sd}/L_{sq} \approx 1$. Thus, the analysis of the AFPM brushless machine with a coreless stator may be done in a similar way as that of the three-phase cylindrical machine with surfaced PMs [128, 157].

5.7 Performance of Coreless Non-Overlap Winding AFPM Machines

The use of non-overlap coils in AFPM electrical machines has certain advantages, amongst other things,

- easier coil manufacture and stator assembly;
- reduced stator winding cost due to less number of coils and simple winding structure;
- smaller overall diameter of the machine due to shorter end-turn length;

Hesai Exhibit 1032, page 173

- lower stator winding losses due to shorter average length of turn;
- higher slot fill factor in the case of slotted stator with ferromagnetic core.

A drawback in general of non-overlap coil machines is the lower output torque due to a lower winding factor expressed by eqns (2.14) and (2.15) [146]. Recent studies, however, shows that non-overlap coil PM machines with high pole numbers can have high winding factors and good output torque [67, 166, 176, 177, 229]. These studies focused on radial flux PM machines with coreless stators. The characterization of an AFPM brushless generator with a coreless non-overlap winding with concentrated parameters is described in [255]. Research work on AFPM machines with coreless non-overlap concentrated parameter windings has been reported in [27, 146, 213]. Coreless AFPM machines with non-overlap windings do not have the problem of cogging torque and of putting the coils into slots. Hence, there is more freedom in the layout and assembly of the winding. Furthermore, non-overlap coil PM machines with ferromagnetic stator core are known for their additional losses in the current conducting PMs and rotor ferromagnetic yoke due to higher harmonic flux pulsations. In coreless non-overlap winding AFPM machines this is almost completely absent due to the low armature reaction effect. There are, thus, no disadvantages in using non-overlap coils with concentrated parameters in coreless stator AFPM machines, except for the lower torque performance in the case of some winding and PM configurations.

In Fig. 5.9 the layouts of overlap and non-overlap windings are shown. Congruent with these layouts, three air-cored AFPM stators (1 kW) with normal overlap, non-overlap and phase-group windings are shown in Fig. 5.10(a)-(c). These stators have been designed and built for the PM rotor discs of the AFPM machine under test shown in Fig. 5.10(d). For the tests an a.c. electromechanical drive has been used as prime mover and a torque transducer to measure the shaft torque as shown in Fig. 5.10(d).

For the numeric modeling of the AFPM machine the 2D FEM analysis has been used. The 2D FEM models of the normal three-phase overlap winding and two types of non-overlap coil AFPM machines are shown in Fig. 5.11. Owing to the axial symmetry, it is only necessary to model half of the machine in the FEM analysis, i.e., one rotor disc and half a stator. For the normal overlap winding AFPM machine, it is possible to model just one pole-pitch of the machine by applying negative periodical condition on the left and right boundaries, as shown in Fig. 5.11(a). However, for the non-overlap winding AFPM machine, it is necessary to model two pole-pairs of the machine by using positive periodical conditions, as shown in Fig. 5.11(b). For the phase-group non-overlap winding AFPM machine, it is inevitable to model the complete machine as there is no symmetry (Fig. 5.11(c)).

The design data of the AFPM machines with different windings is given in Table 5.4. The per unit calculated and measured results of the different winding AFPM machines are given in Table 5.5. The analytically calculated, FEM-calculated and measured results of the overlap winding are throughout

Hesai Exhibit 1032, page 174

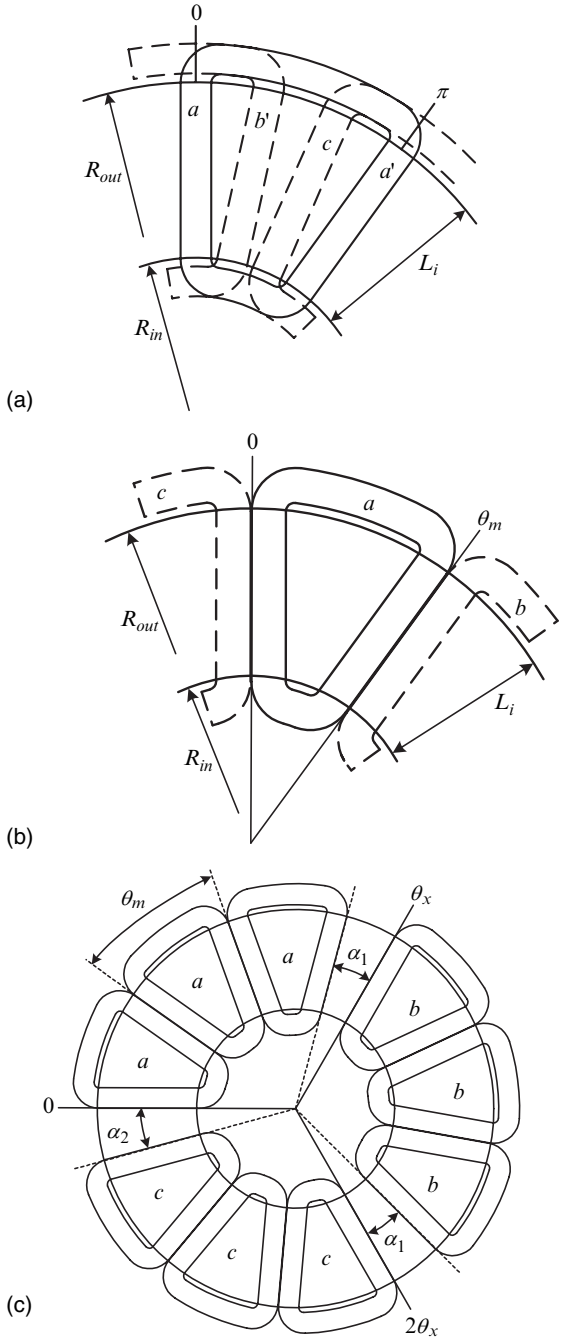


Fig. 5.9. Layout of different coreless windings with (a) normal overlap winding, (b) non-overlap winding, and (c) phase-group non-overlap winding.

Hesai Exhibit 1032, page 175

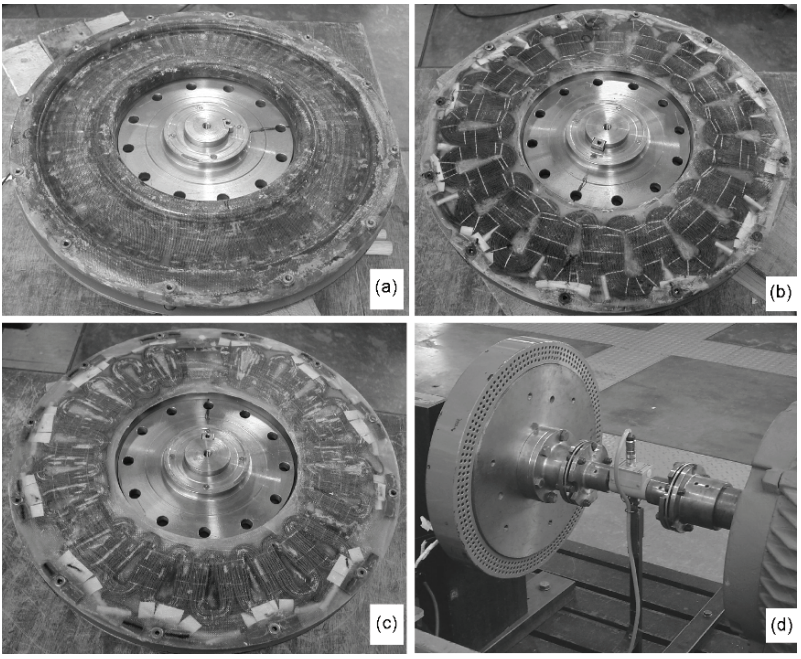


Fig. 5.10. Coreless AFPM machine stators with (a) normal overlap winding, (b) non-overlap winding, (c) phase-group non-overlap winding, and (d) testing set-up of AFPM machine as a generator [146].

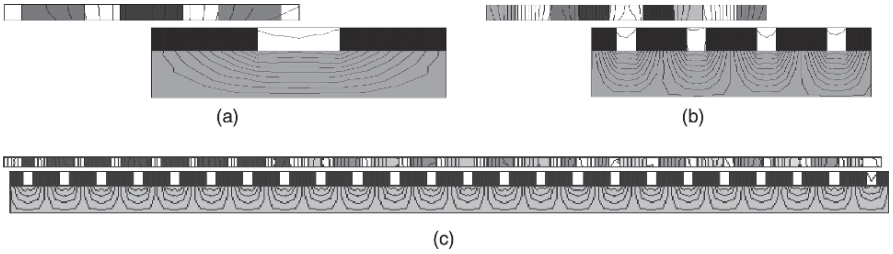


Fig. 5.11. 2D FEM models of coreless AFPM machine with (a) normal overlap, (b) non-overlap winding, and (c) phase-group non-overlap winding [146].

taken as the basis in the per unit calculation. The calculation and measurements were performed for the same copper loss of 120 W for each type of stator winding. It is clear from the results of Table 5.5 that the same torque per copper loss is obtained with the non-overlap winding as with the normal overlap windings. However, non-overlap winding needs significantly less copper.

Hesai Exhibit 1032, page 176

Table 5.4. Design data of AFPM machines with different winding topologies

Design data	overlap	non-overlap	phase-group
Output power P_{out}, kW	1	1	1
Speed n, rpm	200	200	200
Number of phases m_1	3 (Wye)	3 (Wye)	3 (Wye)
Rated line voltage, V	19.88	19.56	18.43
Rated phase current, A	13.79	14.23	13.06
Frequency f, Hz	40	40	40
Number of stator modules	1	1	1
Number of pole pairs p	12	12	12
Number of stator coils (3 phases)	36	18	21
Number of turns per coil	11	25	23
Wire diameter, mm	0.8	0.85	0.7
Number of parallel wires a_w	7	6	6
Axial height of PM h_M, mm	6	6	6
Axial thickness of winding t_w, mm	8.4	8.4	8.4
Air gap (one side) g, mm	1.8	1.8	1.8
Air gap flux density B_{mg}, T	0.527	0.527	0.527
PM outer diameter D_{out}, mm	400	400	400
$k_d = D_{in}/D_{out}$ ratio	0.7	0.7	0.7
Class of insulation	F	F	F
Winding temperature rise, °C	9.9	12.1	8.3
Cooling system	Air-cooled	Air-cooled	Air-cooled

Table 5.5. Comparison of calculated and measured per unit results for AFPM brushless machines with $D_{in} = 280$ mm $D_{out} = 400$ mm and $p = 12$ [146]

			Torque			Mass of copper	
Type	z	Q_c	analytical	FEM	measured	analytical	measured
Overlap	-	36	1	1	1	1	1
Non-overlap	1	18	0.988	1.013	1.014	0.891	0.854
Phase-group	7	21	0.885	0.902	0.899	0.683	0.624

Fig. 5.12 shows the measured induced open circuit voltage of the normal overlap and the non-overlap windings. It is clear that an improved sinusoidal voltage waveform is obtained with the non-overlap winding.

5.8 Eddy Current Losses in the Stator Windings

5.8.1 Eddy Current Loss Resistance

For an AFPM machine with a coreless stator, associated stator iron losses are absent. The rotor discs rotate at the same speed as the main magnetic field, thus the core losses in the rotor discs due to the fundamental harmonic of the stator field also do not exist. However, the eddy current losses in the

Hesai Exhibit 1032, page 177

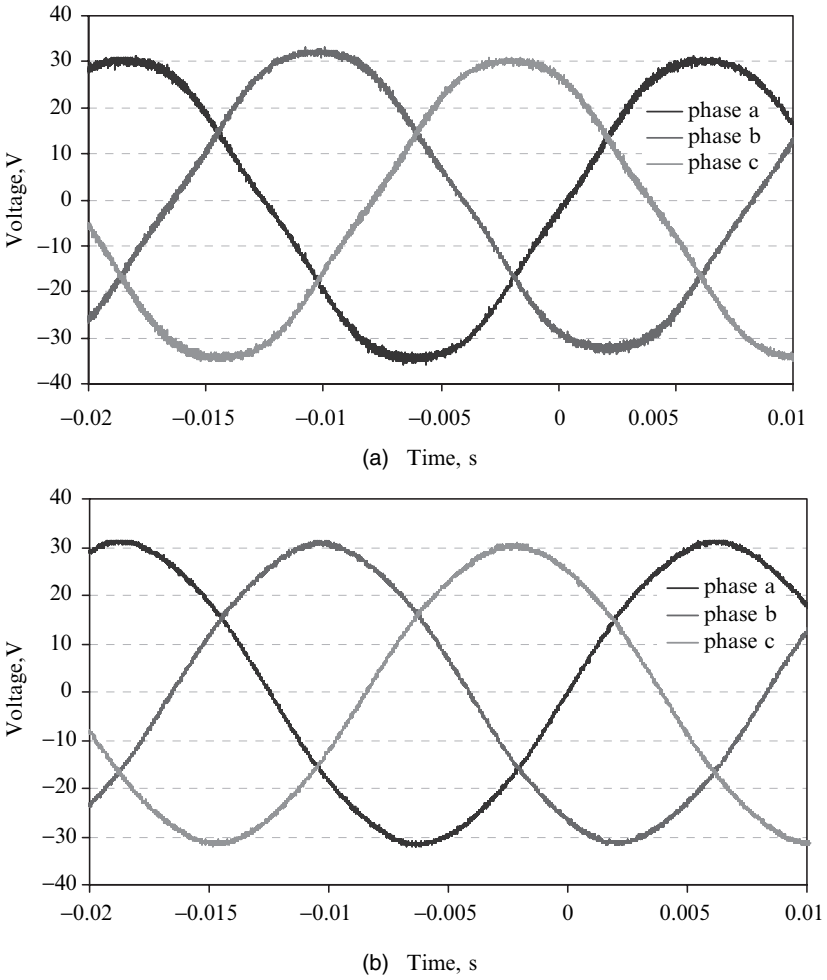


Fig. 5.12. Measured open circuit voltage waveform of AFPM machine with (a) overlap, and (b) non-overlap winding [146].

stator winding are significant due to the fact that the machine is designed with $2p \geq 6$ to operate at relatively high frequencies $f = pn$.

Eddy current losses ΔP_e in stator conductors are calculated according to eqn (2.68) or eqn (2.69). A more detailed method of the eddy current losses computation is discussed in [263]. Eddy current losses in the stator conductors can be accounted for in the same way as core losses in the stator stack [126]. The eddy-loss current I_e and its d- and q-axis components I_{ed} and I_{eq} shown in Fig. 5.5 is in phase with the internal phase voltage E_i across the shunt resistance R_e. The internal phase voltage E_i is generated by the resultant air gap flux and usually referred to as the air gap voltage [94]. Consequently, the

Hesai Exhibit 1032, page 178

shunt resistance in the equivalent circuit representing the eddy current loss is expressed as

$$R_e = m_1 I_e^2 R_e = \frac{m_1 E_i^2}{\Delta P_e} \tag{5.32}$$

where

$$I_e = \sqrt{I_{ed}^2 + I_{eq}^2} \tag{5.33}$$

On the basis of equivalent circuits (Fig. 5.5), the following equations can be written in the phasor form:

- for generators

$$\mathbf{E}_f = \mathbf{E}_i + j\mathbf{I}_{ad}X_{ad} + j\mathbf{I}_{aq}X_{aq} \tag{5.34}$$

$$\mathbf{I}'_a = \mathbf{I}_a + \mathbf{I}_e \tag{5.35}$$

- for motors

$$\mathbf{E}_f = \mathbf{E}_i - j\mathbf{I}_{ad}X_{ad} - j\mathbf{I}_{aq}X_{aq} \tag{5.36}$$

$$\mathbf{I}'_a = \mathbf{I}_a - \mathbf{I}_e \tag{5.37}$$

where $\mathbf{I}'_a$ is the stator current with eddy currents being accounted for and $\mathbf{I}_a$ is the stator current with eddy currents being ignored.

5.8.2 Reduction of Eddy Current Losses

In an AFPM machine with a coreless stator the winding is directly exposed to the air gap magnetic field (see Fig. 5.13). Motion of PMs over the coreless winding produces an alternating field through each conductor inducing eddy currents. The loss due to eddy currents in the conductors depends on both the geometry of the wire cross section and the amplitude and waveform of the flux density. In order to minimize the eddy current loss in the conductors, the stator winding should be designed in one of the following ways using:

- parallel wires with smaller cross sections instead of a one thick conductor;
- stranded conductors (Litz wires);
- coils made of copper or aluminum ribbon (foil winding).

In an AFPM machine with an ironless winding arrangement (as shown in Fig. 5.13a), in addition to its normal component, the air gap magnetic field has a tangential component, which can lead to serious additional eddy current loss (Fig. 5.13b). The existence of a tangential field component in the air gap discourages the use of ribbon conductors as a low cost arrangement. Litz wires

Hesai Exhibit 1032, page 179

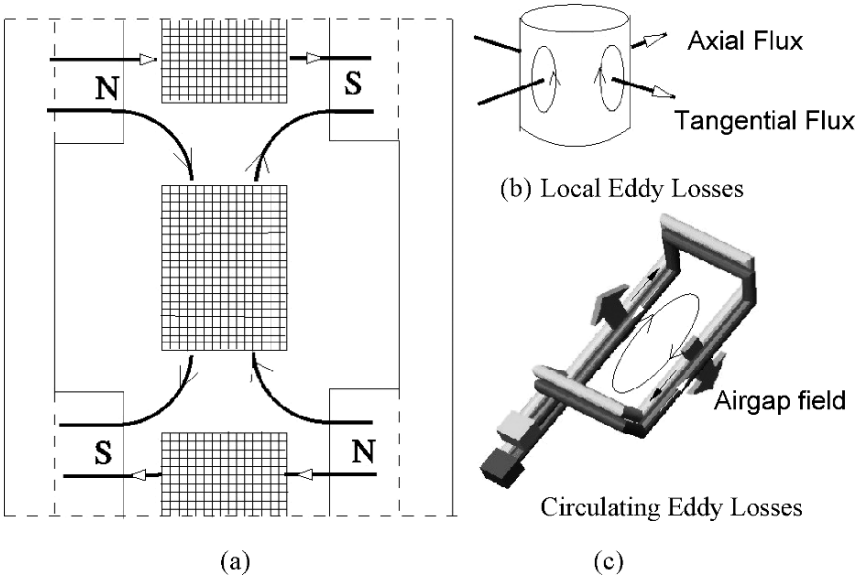


Fig. 5.13. Eddy currents in the coreless stator winding of an AFPM machine: (a) magnetic field distribution in a coreless stator; (b) eddy currents in a conductor; (c) circulating eddy currents among parallel connected conductors.

allow significant reduction of eddy current loss, but they are more expensive and have fairly poor filling factors.

As a cost effective solution, a bunch of parallel thin wires can be used. However, this may create a new problem, i.e. unless a complete balance of induced EMFs among the individual conducting paths is achieved, a circulating current between any of these parallel paths [161, 231, 263] may occur as shown in Fig. 5.13c, causing circulating eddy current losses.

When operating at relatively high frequency magnetic fields, these eddy current effects may cause a significant increase of winding losses, which are intensified if there are circulating currents among the parallel circuits. These losses will deteriorate the performance of the AFPM brushless machine. Predicting the winding eddy current losses with a good accuracy is therefore very important at the early stage of design of such machines.

Eddy current losses may be resistance limited when the flux produced by the eddy currents has a negligible influence on the total field [231]. In this case the conductor dimensions (diameter of thickness) are small when compared to the equivalent depth of penetration $\Delta = 1/k_\nu$ of the electromagnetic field – eqn (1.17).

Hesai Exhibit 1032, page 180

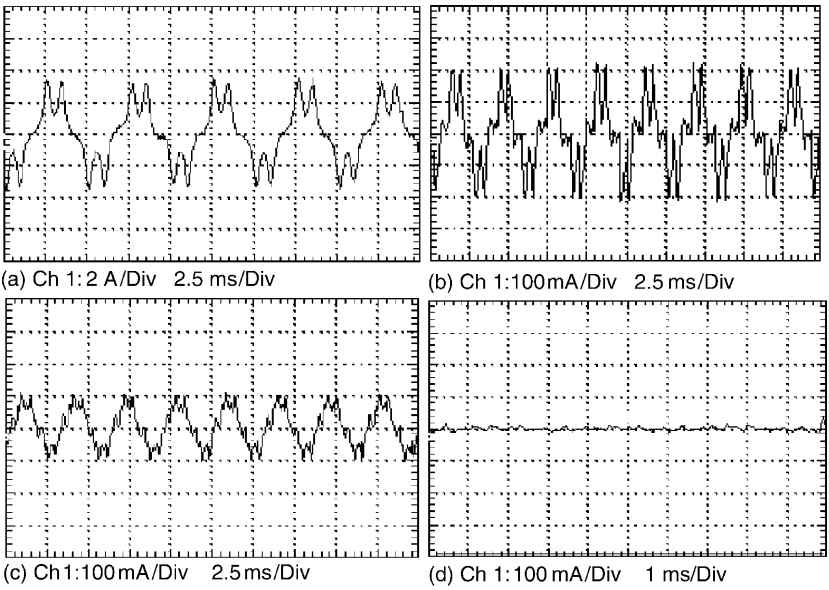


Fig. 5.14. Measured circulating current of (a) non-twisted coil, (b) slightly twisted coil, (c) moderately twisted coil, (d) heavily twisted coil.

5.8.3 Reduction of Circulating Current Losses

To minimise the circulating current in a coil made of parallel conductors, the normal practice is to twist or transpose the wires in such a fashion that each parallel conductor occupies all possible layer positions for the same length of the coil. The effect is to equalize the induced EMFs in all parallel conductors, and to allow them to be paralleled at the ends without producing eddy circulating currents between the parallel conductors.

Figure 5.14 illustrates the effectiveness of suppressing circulating eddy current by wire twisting. Four coils are made with the only difference that the parallel wires of each coil are: (a) non-twisted, (b) slightly twisted (10 to 15 turns per metre), (c) moderately twisted (25 to 30 turns per metre), and (d) heavily twisted (45 to 50 turns per metre) respectively. All the coils have been used to form a portion of an experimental stator, which is placed in the middle of the two opposing PM rotor discs. The machine operates at a constant speed (400 rpm in this case). The circulating currents between two parallel conductors have been measured and logged on a storage oscilloscope. It can be seen that the induced circulating current is greatly reduced even with a slightly twisted coil and can generally be ignored in a heavily twisted coil. These twisted wires can easily be manufactured in a cost effective way.

The fill (space) factors for the non-twisted and the heavily twisted coils are estimated as 0.545 and 0.5 respectively, which is slightly less than that of the

Hesai Exhibit 1032, page 181

Litz wires (typically from 0.55 to 0.6). However, the saving in manufacturing costs is more important.

It should be noted that due to the low impedance of a coreless stator winding, circulating current could also exist among coil groups connected in parallel (parallel current paths) if a perfect symmetry of coils cannot be guaranteed.

5.8.4 Measurement of Eddy Current Losses

The resistance limited eddy loss in the stator of an AFPM machine may be experimentally determined by measuring the difference in input shaft powers of the AFPM machine at the same speed, first with the stator in, and then by replacing it with a dummy stator (no conductors). The dummy stator has the same dimensions and surface finish as the real stator and is meant to keep the windage losses the same.

A schematic representation of the experimental test setup for measuring eddy current losses in stator conductors is shown in Fig. 5.15. The shaft of the tested prototype and the shaft of the prime mover (driving machine) are coupled together via a torque meter. The stator is positioned in the middle of the two rotor discs with the outer end ring (see Fig. 5.15a) mounted on the outside supporting frame. Temperature sensors are also attached to the conductors in order to take into account temperature factor in the measurement.

Initially, the prototype (with the coreless stator placed in it) was driven by a variable speed motor for a number of different speeds. The corresponding torque measurements were taken. Replacing the real stator with a dummy one, the tests were repeated for the same speeds. Both the torque and the temperature values were recorded. The difference of the torques multiplied by the speed gives the eddy current loss. The eddy losses due to eddy-circulating current in the windings can also be determined by measuring the difference of input shaft powers, first with all the parallel circuits connected and then with disconnected parallel circuits.

Fig. 5.16 shows the measured and calculated resistance limited eddy losses of the prototype machine. It can be seen that the calculated eddy losses obtained by using the standard analytical formula – eqns (2.68) and (2.69) with only the B_{mz} component taken into account yield underestimated values (43% less). The discrepancy between the measured and calculated results becomes large at high speeds. Better accuracy may be achieved by including both the normal B_{mz} and tangential B_{mx} components of the magnetic flux density and implementing eqn (2.68) or eqn (2.69) into the 2D or 3D FEM [262].

5.9 Armature Reaction

The 3-D FEM analysis has been applied to the modelling of a coreless stator AFPM machine in [10]. Both no-load and load operations have been modelled. It has been shown that good accuracy can be expected even when the

Hesai Exhibit 1032, page 182

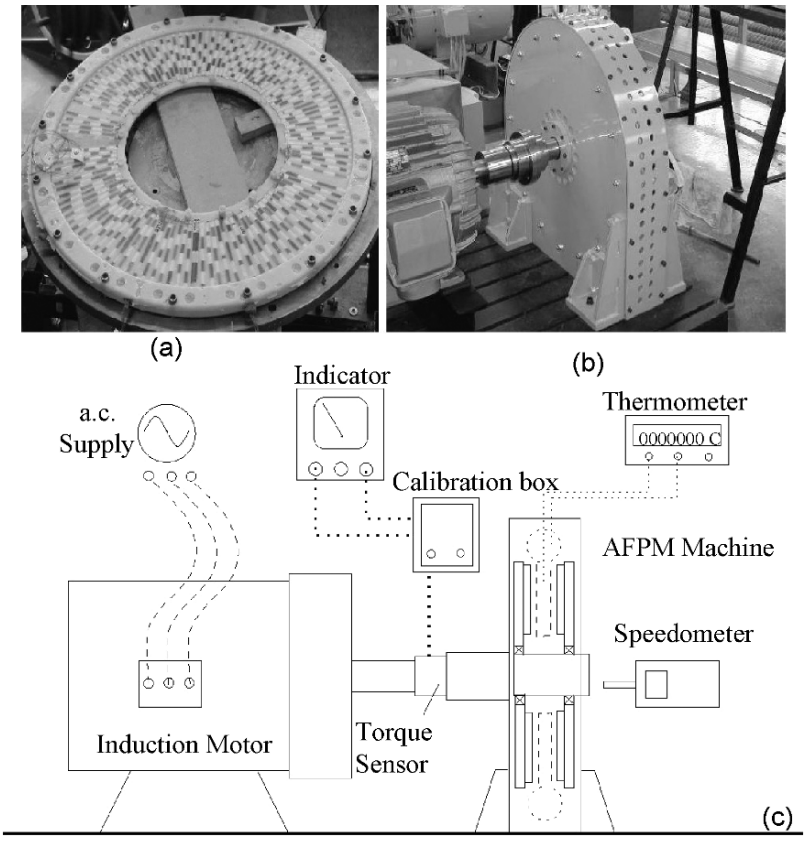


Fig. 5.15. Laboratory set for measuring eddy current losses in the stator winding: (a) specially designed stator; (b) experimental machine; (c) schematic of experimental set-up.

first order linear FEM solution is applied to the AFPM machine if the magnetic circuit is not saturated (large air gap). It has also been found that the armature reaction for an AFPM machine with a coreless stator is generally negligible.

Using a 40-pole, 766 Hz coreless stator AFPM machine as an example, the simulated effects of armature reaction to the air gap flux distribution has been demonstrated in Figs 5.17 and 5.18. It can be seen that the plateau of the axial field plot is somewhat tilted due to the interaction between the flux of the PMs and the armature flux generated by the rated current (Fig. 5.17). Similarly, the modified tangential field plot is compared with the original one in Fig. 5.18.

As the armature reaction flux is small in coreless AFPM machines with large air gaps, the air gap magnetic flux density maintains its maximum value very

Hesai Exhibit 1032, page 183

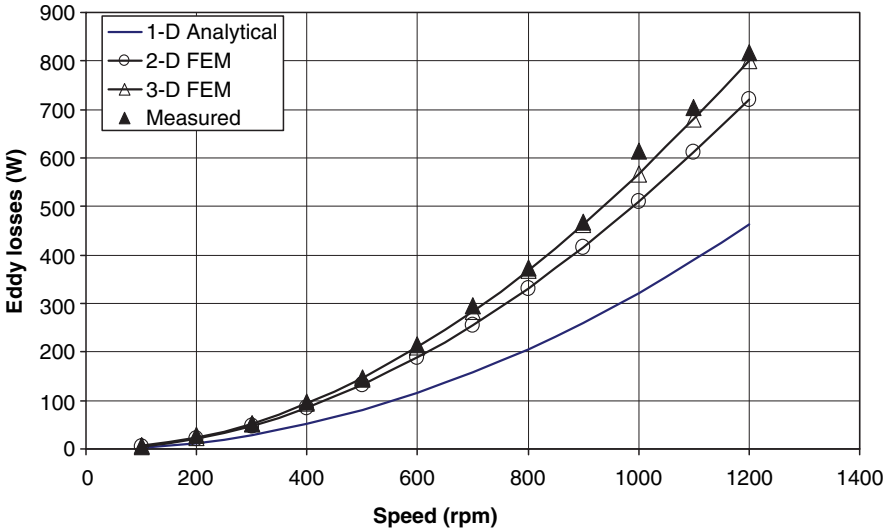


Fig. 5.16. Comparison of calculated eddy loss with measurements.

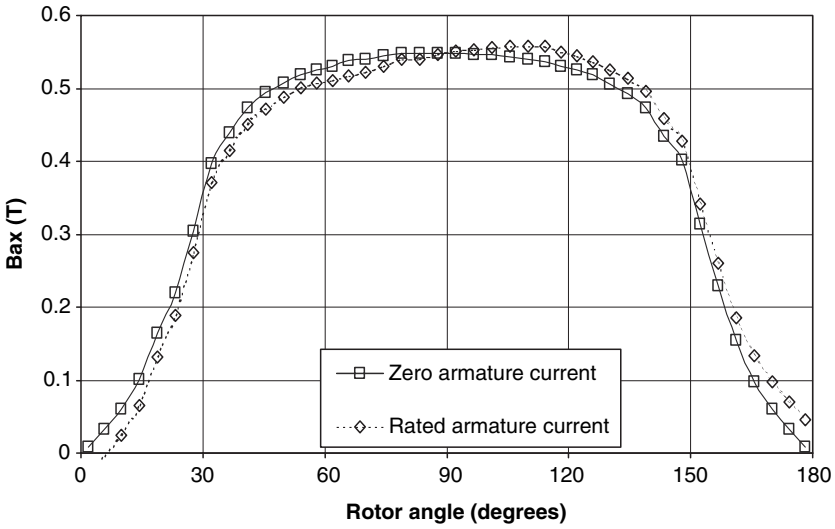


Fig. 5.17. Air gap axial field component at no-load and full load conditions.

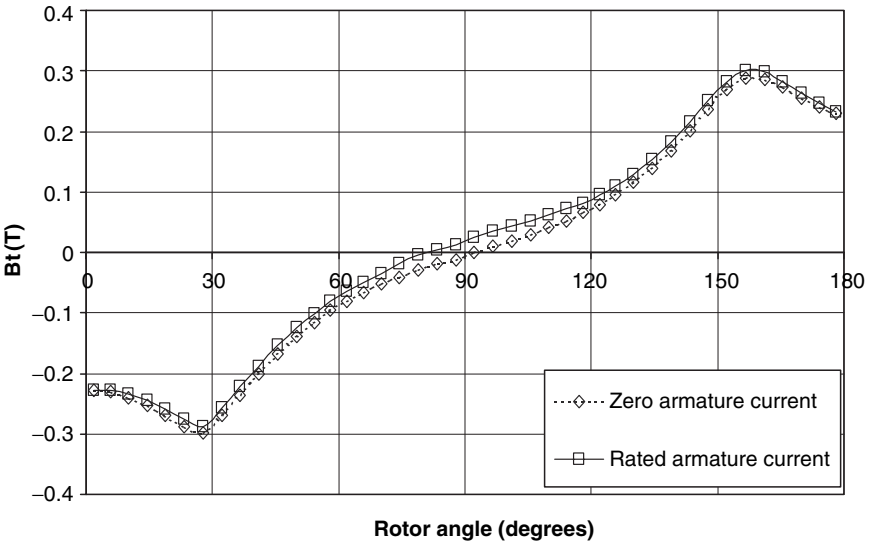


Fig. 5.18. Air gap tangential field component at no-load and full load conditions.

close to that at no load. The influence of the armature reaction on the eddy current losses is usually insignificant though it can be easily accounted for when the FEM modelling is used. The harmonic contents of the air gap flux density obtained with and without armature reaction are compared in Table 5.6. It is evident that, in this case, the change of the field harmonic composition due to the armature reaction is negligible.

Table 5.6. Harmonics content of the axial air-gap flux density with and without armature reaction

Harmonics	Rated armature current	Zero armature current
1^{st}	0.60346784	0.60246033
3^{nd}	0.03745651	0.03745759
5^{rd}	0.04099061	0.04070525
7^{th}	0.03502689	0.03514609
9^{th}	0.01231397	0.01230032
11^{th}	0.00304573	0.00262309
13^{th}	0.00559543	0.00579739
15^{th}	0.00314908	0.00312179
17^{th}	0.00083159	0.00086812
19^{th}	0.00307828	0.00272939

Hesai Exhibit 1032, page 185

5.10 Mechanical Design Features

In the mechanical design of an AFPM brushless machine, obtaining a uniform air gap between the rotor disc and the stator is important. Therefore, the methods of fixing the rotor discs onto the shaft and the stator onto the enclosure (frame) are very important. Improper methods of fixing, or misalignment in the assembling of the stator and rotor will cause a nonuniform air gap, vibration, noise, torque pulsation and deterioration of electrical performance.

With regard to cooling in an air-cooled AFPM machine, the entry losses of the air flow can be quite high if the machine-air-inlet is poorly designed. It is important to reduce these losses without weakening the mechanical structure for better cooling.

To summarise, attention should be paid to the following aspects of the mechanical design:

- **Shaft**. The load torque, the first critical speed and the shaft dynamics should be taken into account in the shaft design.
- **Rotor**. (i) The deflection of the rotor disc due to the strong magnetic attraction force, (ii) the means of mounting and securing the magnets on the rotor discs to counteract the strong centrifugal force especially for high speed applications, and (iii) the balancing of the rotor discs.
- **Stator**. (i) The strength and rigidity of the resin reinforced stator and frame, and (ii) the positioning and spacing of the coils to ensure perfect symmetry.
- **Cooling**. For air cooled AFPM machines, the air inlet and air flow paths through the machine should be carefully designed in order to ensure a better mass flow rate and therefore better cooling.
- **Assembly**. An effective tool to facilitate the assembling and dismantling of the machine for maintenance.

5.10.1 Mechanical Strength Analysis

The deflection of the rotor discs due to the strong magnetic pull may have the following undesirable effects on the operation and condition of AFPM machines:

- closing the running clearance between the rotor disc and the stator;
- loose or broken PMs;
- reducing air-flow discharging area thus deteriorating the cooling capacity;
- nonuniform air gap causing a drift in electrical performance from the optimum.

For a double-sided AFPM machine with an internal coreless stator, the rotor discs account for roughly 50% of the total active mass of an AFPM machine. Hence, the optimal design of the rotor discs is of great importance to realise a design of high power–to–mass ratio. All these aspects require the mechanical stress analysis of the rotor disc.

Hesai Exhibit 1032, page 186

Attraction Force between Rotor Discs

The attraction force between two parallel rotor discs can be calculated by using the *virtual work* method, i.e.

$$F_z = -\frac{dW}{dz} \approx -\frac{\Delta W}{\Delta z} = -\frac{W_2 - W_1}{z_2 - z_1} \tag{5.38}$$

where W is the total magnetic energy stored in the machine and Δx is the small variation of the air gap length. The accurate prediction of the attraction force is a prerequisite for the mechanical stress analysis. Hence, the respective magnetic stored energies W_1 and W_2 for air gap lengths z_1 and z_2 are usually calculated by using the FEM.

Analytically, the normal attractive force between two parallel discs with PMs can be expressed as

$$F_z \approx \frac{1}{2}\frac{B_{mg}^2}{\mu_0} S_{PM} \tag{5.39}$$

where the active area of PMs is according to eqn (2.63).

Optimum Design of Rotor Discs

The structure of the rotor steel discs may be optimised with the aid of an FEM structural program. It is important that the deflection of the rotor steel discs, due to the axial magnetic pull force, is not too dangerous for small running clearance between the coreless stator and PMs. Two important constraints should be considered, i.e. (i) the maximum allowable deflection and (ii) the maximum mechanical strength of the material used to fabricate the disc.

When choosing allowable deflection, one needs to make sure that the PMs do not experience any excessive forces due to bending of the disc that can potentially peel them off from the backing steel disc. Owing to the cyclical symmetry of the disc structures, it is sufficient to model only a section of the disc with symmetry boundary conditions applied. In the FEM analysis the axial magnetic force can be applied in the form of a constant pressure load over the total area that the PMs occupy. Usually, the axial-symmetric elements are preferred for modelling a relatively thick disc. However, it has been shown in [182] that the FEM modelling of rotor discs using both axial-symmetric-elements and shell-elements gives very close results.

Fig. 5.19 shows the finite element model of the analysed rotor disc using 4-node shell-elements, with symmetrical boundary conditions applied. The axial magnetic attraction force has been calculated as 14.7 kN and applied in the form of a constant 69.8 kPa pressure load. Specification of the investigated AFPM machine are given in Table 5.3. The stiffness provided by the magnets has not been included, to keep the design on the conservative side. As the rotor discs are mounted on the centre support hub, additional boundary constraints

Hesai Exhibit 1032, page 187

have been defined so that there is no axial displacement in the vicinity of the mounting bolts and contact area.

To find the suitable thickness of the rotor disc, which satisfies the critical strength requirements of the rotor disc with a low steel content, the linear FEM static analysis was performed for different thicknesses of the rotor disc.

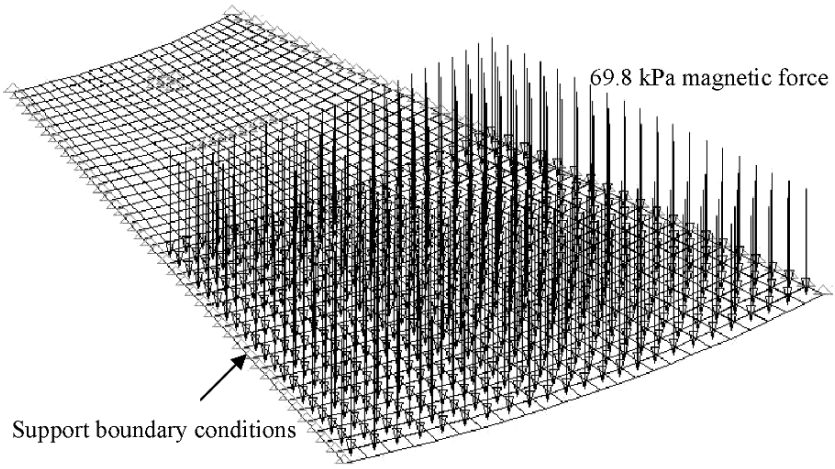


Fig. 5.19. FEM model for analysing the mechanical stress of the rotor disc.

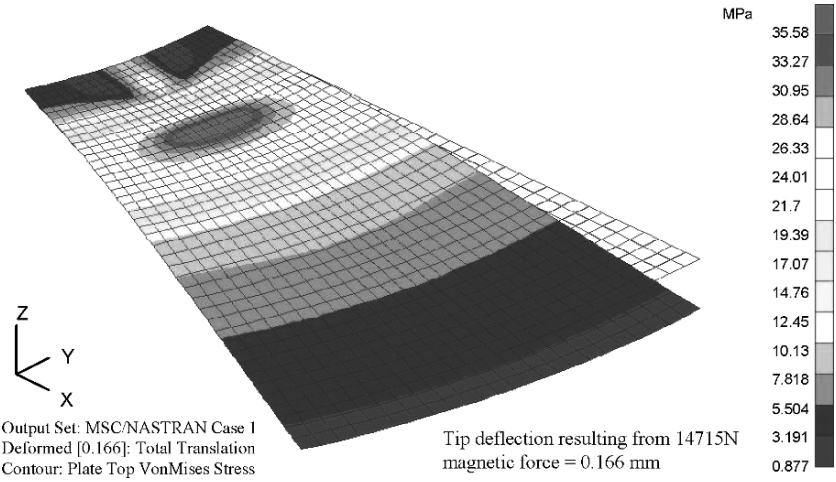


Fig. 5.20. Deflection (blown-up) and von Mises stress distribution of the rotor disc.

Hesai Exhibit 1032, page 188

Based on the analysis, the rotor disc thickness was chosen as 17 mm with a maximum deflection of 0.145 mm. Fig. 5.20 shows the deflection (blown-up) and the von Mises stress distribution of the laboratory prototype of the 17-mm thick disc. The maximum stress of 35.6 MPa is much lower than the typical yield strength of mild steel, that is in the region of 300 MPa. It has been shown in literature [182] that the bending of the rotor disc decreases towards its outer periphery. The rotor disc may be machined in such a way that the disc becomes thinner towards the outer periphery. As shown in Table 5.7, the tapered disc uses approximately 10% less steel than the straight disc. The maximum deflection increases by only 0.021 mm with the tapered disc, which is negligible. This can effectively reduce the active mass of the machine without compromising the mechanical strength, but does not bring down the cost of the steel.

If manufacturing costs are taken into account for small production volumes, it is better to use a steel disc with uniform thickness. Obviously, a uniform disc means a heavier rotor disc. It can, however, be argued that the extra machining work needed for producing a tapered rotor disc may be too costly to justify the profit due to improvement in the dynamic performance. As long as the added mass can be tolerated, this option is viable for small production volumes and for laboratory prototypes.

Table 5.7. Comparison of different designs of rotor disc

Parameter	Straight disc	Tapered disc
Mass, kg	39.184	31.296
Maximum deflection, mm	0.145	0.166
Maximum von Mises stress, MPa	35.6	33.4

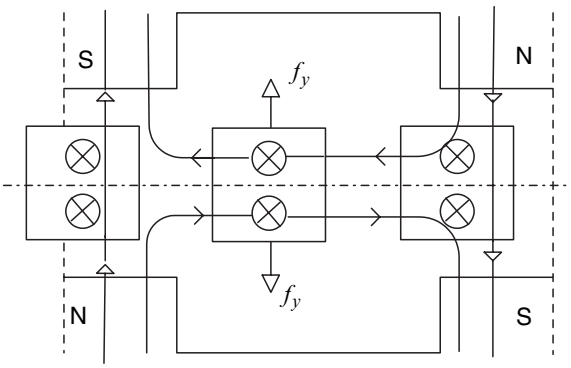


Fig. 5.21. Schematic diagram showing the axial force exerted on stator.

Hesai Exhibit 1032, page 189

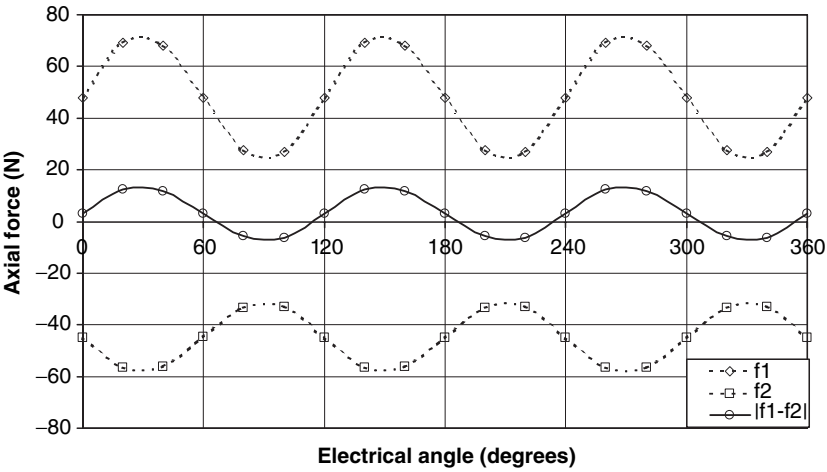


Fig. 5.22. Unbalanced axial force exerted on the stator.

5.10.2 Imbalanced Axial Force on the Stator

As a result of the interaction of alternating currents in conductors and the tangential component of the magnetic field, there is an axial magnetic force f_z on each half of the coil as shown in Fig. 5.21. When the stator is located in the middle of the air gap, the forces on each side of the stator should cancel each other.

Assuming that the coreless stator of the AFPM machine is slightly off centre, the axial forces on each side of the stator (f_1 and f_2) as shown in Fig. 5.22 will not be the same, resulting in an unbalanced force, $\Delta f = |f_1 - f_2|$, being exerted on the stator. This unbalanced force may cause extra vibration and thus have an adverse effect on the mechanical strength of the epoxy reinforced stator.

5.11 Thermal Problems

Owing to the excessive heat generated in the stator winding and the resultant thermal expansion, an epoxy encapsulated stator is subject to certain deformation. When the deformation is significant, it may cause physical contact between the stator and the magnets resulting in serious damage to the stator winding and the magnets.

Fig. 5.23 shows the thermal expansion of the stator at different temperatures. The rated current (16 A) has been conducted through a coil in the epoxy encapsulated stator. A thermal coupler and a roundout meter have been used to measure the coil temperature and surface deformation respectively. It

Hesai Exhibit 1032, page 190

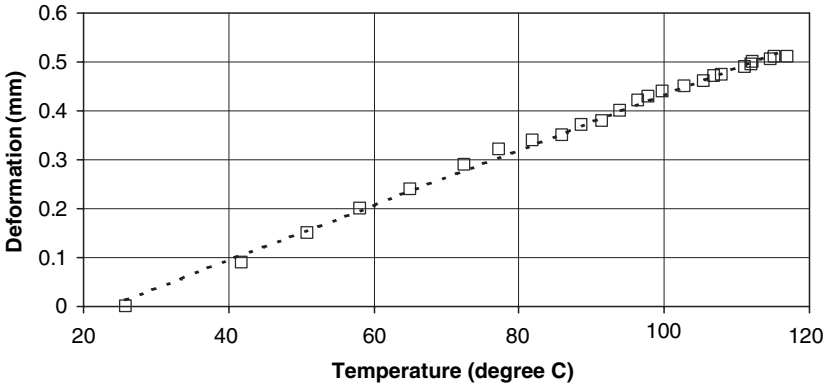


Fig. 5.23. Thermal expansion of the stator for different temperatures.

has been found that the relationship between the stator deformation and its temperature is almost linear. On average, the deflection of the stator surface is about 0.0056 mm/°C, resulting in a 0.5 mm deflection at the temperature of 117°C. The remaining air contents in the epoxy can also contribute to the heat transfer deterioration and temperature increase. To solve this problem, a more dedicated production process is suggested. The running clearance between the stator and the rotor should be kept reasonably large.

Numerical Example 5.1

A three-phase, Y-connected, 3000 rpm PM disc motor has a coreless stator and twin external rotor with surface PMs and backing steel discs. Sintered NdFeB PMs with $B_r = 1.2$ T and $\mu_{rrec} = 1.045$ have been used. The nonmagnetic distance between opposite PMs is $t = 11$ mm, the winding thickness is $t_w = 8$ mm and the height of PMs (in axial direction) is $h_M = 6$ mm. The outer diameter of PMs equal to the outer diameter of the stator conductors is $D_{out} = 0.22$ m and the parameter $k_d = 1/\sqrt{3}$. The number of poles is $2p = 6$, the number of single layer coil sides (equivalent to the number of slots) is $s_1 = 54$, the number of turns per phase is $N_1 = 234$, the number of parallel conductors $a_w = 2$, the diameter of wire $d_w = 0.912$ mm (AWG 19) and the coil pitch is $w_c = 7$ coil sides.

Find the motor steady state performance, i.e. output power, torque, efficiency and power factor assuming that the total armature current $I_a = 8.2$ A is torque producing ($I_{ad} = 0$). The saturation factor of the magnetic circuit is $k_{sat} = 1.02$, the motor is fed with sinusoidal voltage, the mass of the twin rotor $m_r = 3.4$ kg, the mass of shaft $m_{sh} = 0.64$ kg, the radius of shaft $R_{sh} = 15$ mm, the conductivity of copper conductors $\sigma = 47 \times 10^6$ S/m at 75°C, the specific density of copper conductors $\rho = 8800$ kg/m^3, the density of PMs $\rho_{PM} = 7700$ kg/m^3, the air density $\rho = 1.2$ kg/m^3, the dynamic viscosity of

Hesai Exhibit 1032, page 191

air $\mu = 1.8 \times 10^{-5}$ Pa s, the coefficient of bearing friction $k_{fb} = 1.5$ and the coefficient of distortion of the magnetic flux density $\eta_d = 1.15$. Losses in PMs, losses in steel rotor discs and the tangential component of the magnetic flux density in the air gap are negligible.

Solution

The number of coils per phase for a single layer winding is $n_c = s_1/(2m_1) = 54/(2 \times 3) = 9$. The number of turns per coil is $N_{ct} = N_1/n_c = 234/9 = 26$. The number of coil sides per pole per phase (equivalent to the number of slots per pole per phase) $q_1 = s_1/(2pm_1) = 54/(6 \times 3) = 3$.

The air gap (mechanical clearance) is $g = 0.5(t - t_w) = 0.5(11 - 8) = 1.5$ mm and the pole pitch measured in coil sides is $\tau_c = s_1/(2p) = 54/6 = 9$.

The input frequency at 3000 rpm is

$$f = n_s p = \frac{3000}{60} \times 3 = 150 \text{ Hz}$$

The magnetic voltage drop equation per pole pair is

$$4\frac{B_r}{\mu_0 \mu_{rrec}} h_M = 4\frac{B_{mg}}{\mu_0}\left[\frac{h_M}{\mu_{rrec}} + \left(g + \frac{1}{2}t_w\right)k_{sat}\right]$$

Hence

$$B_{mg} = \frac{B_r}{1 + [\mu_{rrec}(g + 0.5t_w)/h_M]k_{sat}}$$

$$= \frac{1.2}{1 + [1.045(1.5 + 0.5 \times 8)/6] \times 1.02} = 0.607 \text{ T}$$

The magnetic flux according to eqn (2.28) is

$$\Phi_f = \frac{1}{8}\frac{2}{\pi}\frac{\pi}{3} 0.607 \times 0.22^2 \left[1 - \left(\frac{1}{\sqrt{3}}\right)^2\right] = 0.001632 \text{ Wb}$$

The winding factor according to eqns (2.8), (2.9) and (2.10) is

$$k_{d1} = \frac{\sin \pi/(2 \times 3)}{3 \sin \pi/(2 \times 3 \times 3)} = 0.9598; \qquad \beta = \frac{w_c}{\tau_c} = \frac{7}{9}$$

$$k_{p1} = \sin\left(\frac{7}{9}\frac{\pi}{2}\right) = 0.9397 \qquad k_{w1} = 0.9598 \times 0.9397 = 0.9019$$

The EMF constant according to eqn (2.37) and torque constant according to eqn (2.34) are respectively

Hesai Exhibit 1032, page 192

$$k_E = \pi\sqrt{2} \times 3 \times 234 \times 0.9019 \times 0.001632 = 4.591 \text{ V/(rev/s)} \; = \; 0.0765 \text{ V/rpm}$$

$$k_T = k_E \frac{m_1}{2\pi} = 4.591 \frac{3}{2\pi} = 2.192 \text{ Nm/A}$$

The EMF at 3000 rpm is

$$E_f = k_E n = 0.0765 \times 3000 = 229.5 \text{ V}$$

The electromagnetic torque at $I_a = I_{aq} = 8.2$ A is

$$T_d = k_T I_a = 2.192 \times 8.2 = 17.97 \text{ Nm}$$

The electromagnetic power is

$$P_{elm} = 2\pi n T_d = 2\pi \frac{3000}{60} \times 17.97 = 5646.8 \text{ W}$$

The inner diameter $D_{in} = D_{out}/\sqrt{3} = 0.22/\sqrt{3} = 0.127$ m, the average diameter $D = 0.5(D_{out} + D_{in}) = 0.5(0.22 + 0.127) = 0.1735$ m, the average pole pitch $\tau = \pi 0.1735/6 = 0.091$ m, the length of conductor (equal to the radial length l_M of the PM) $L_i = l_M = 0.5(D_{out} - D_{in}) = 0.5(0.22 - 0.127) = 0.0465$ m, the length of shorter end connection without inner bends $l_{1emin} = (w_c/\tau_c)\pi D_{in}/(2p) = (7/9)\pi \times 0.127/6 = 0.052$ m and the length of the longer end connection without outer bends $l_{1emax} = 0.052 \times 0.22/0.127 = 0.0896$ m.

The average length of the stator turn with 15-mm bends (Fig. 3.16) is

$$l_{1av} \approx 2L_i + l_{1emin} + l_{1emax} + 4 \times 0.015$$

$$= 2 \times 0.0465 + 0.052 + 0.0896 + 0.06 = 0.2943 \text{ m}$$

The stator winding resistance at 75°C according to eqn (2.40) is

$$R_1 = \frac{234 \times 0.2943}{47 \times 10^6 \times 2 \times \pi \times (0.912 \times 10^{-3})^2/4} = 1.122 \; \Omega$$

The maximum width of the coil at the diameter D_{in} is $w_w = \pi D_{in}/s_1 = \pi 0.127/54 = 0.0074$ m $= 7.4$ mm. The thickness of the coil is $t_w = 8$ mm. The number of conductors per coil is $N_c = a_w \times N_{ct} = 2 \times 26 = 52$. The maximum value of the coil packing factor is at D_{in}, i.e.

$$k_{fmax} = \frac{d_w^2 \times N_c}{t_w w_w} = \frac{0.912^2 \times 52}{8 \times 7.4} = 0.732$$

The stator current density is

$$j_a = \frac{8.2}{2 \times \pi 0.912^2/4} = 6.28 \text{ A/mm}^2$$

Hesai Exhibit 1032, page 193

The stator winding losses according to eqn (2.49) are

$$\Delta P_{1w} = 3 \times 8.2^2 \times 1.122 = 226.2 \text{ W}$$

The eddy current losses in stator round conductors according to eqn (2.68) are

$$\Delta P_e = \frac{\pi^2}{4} \frac{47 \times 10^6}{8800} 150^2 \times 0.000912^2 \times 0.75 \times 0.607^2 \times 1.15^2 = 90.2 \text{ W}$$

where the mass of stator conductors (radial parts) is

$$m_{con} = \rho_{cu} m_1 a_w N_1 \left(\frac{\pi d_w^2}{4} \right) (2L_i)$$

$$= 8800 \times 3 \times 2 \times 234 \left(\frac{\pi 0.000912^2}{4} \right) (2 \times 0.0465) = 0.75 \text{ kg}$$

The friction losses in bearings according to eqn (2.71) are

$$\Delta P_{fr} = 0.06 \times 1.5(3.4 + 0.64) \frac{3000}{60} = 18.2 \text{ W}$$

The windage losses according to eqn (2.74) are

$$\Delta P_{wind} = \frac{1}{2} 7.353 \times 10^{-3} \times 1.2 \left(2\pi \frac{3000}{60} \right)^3 [(0.5 \times 0.115)^5 - (0.5 \times 0.015)^5] \approx 2.8 \text{ W}$$

where

$$R'_{out} \approx 0.5 D_{out} + 0.005 = 0.5 \times 0.22 + 0.005 = 0.115 \text{ m}$$

$$Re = 1.2 \frac{2\pi(3000/60)}{1.8 \times 10^{-5}} \times 0.115^2 = 2.77 \times 10^5$$

$$c_f = \frac{3.87}{\sqrt{2.77 \times 10^5}} = 7.353 \times 10^{-3}$$

The rotational (mechanical) losses according to eqn (2.70) are

$$\Delta P_{rot} = 18.2 + 2.8 = 21 \text{ W}$$

The output power is

$$P_{out} = P_{elm} - \Delta P_{rot} = 5646.8 - 21 = 5625.8 \text{W}$$

The shaft torque is

Hesai Exhibit 1032, page 194

$$T_{sh} = \frac{5625.8}{2\pi \times 3000/60} = 17.91 \text{ Nm}$$

The input power is

$$P_{in} = P_{elm} + \Delta P_{1w} + \Delta P_e = 5646.8 + 226.2 + 90.2 = 5963.2 \text{ W}$$

The efficiency is

$$\eta = \frac{5625.8}{5963.2} = 0.943$$

The leakage reactance can be approximately calculated taking into account the radial part of conductors, end connection and differential leakage fluxes, i.e.

$$\lambda_{1e} \approx 0.3q_1 = 0.3 \times 3 = 0.9 \qquad \lambda_{1s} \approx \lambda_{1e} = 0.9$$

$$\lambda_{1d} = \frac{3 \times 3 \times 0.091 \times 0.9019^2}{\pi^2(2 \times 0.0015 + 0.008)1.02} \times 0.011 = 0.066$$

where according to eqn (4.23), the differential leakage factor $\tau_{d1} = 0.011$ for $5 \le \nu \le 997$.

The stator leakage reactance is

$$X_1 = 4\pi \times 0.4\pi \times 10^{-6} \times 150 \frac{234^2 \times 0.0465}{3 \times 3} \left(0.9 + \frac{0.071}{0.0465} \times 0.9 + 0.066\right)$$

$$= 1.564 \ \Omega$$

where the average length of one end connection is $l_{1e} = 0.5(l_{1emin} + l_{1emax}) = 0.5(0.052 + 0.0896) = 0.071$ m.

The equivalent air gap in the d axis according to eqn (2.112) is

$$g' = 2\left[(1.5 + 0.5 \times 8)1.02 + \frac{6}{1.045}\right] = 22.7 \text{ mm}$$

The equivalent air gap in the q axis according to eqn (2.113) is

$$g'_q = 2[(1.5 + 0.5 \times 8) + 6] = 23 \text{ mm}$$

Armature reaction reactances according to eqns (2.121) and (2.122) are

$$X_{ad} = 2 \times 3 \times 0.4 \times \pi \times 10^{-6} \times 150 \left(\frac{234 \times 0.9019}{3}\right)^2 \frac{1}{0.0227}$$

$$\times[(0.5 \times 0.22)^2 - (0.5 \times 0.127)^2] = 1.989\ \Omega$$

$$X_{aq} = X_{ad}\frac{22.7}{23.0} = 1.963\ \Omega$$

where $k_{fd} = k_{fq} = 1$ for surface configuration of PMs [106].

Synchronous reactances according to eqns (2.79) and (2.80) are respectively

$$X_{sd} = 1.543 + 1.989 = 3.532\ \Omega$$

$$X_{sq} = 1.543 + 1.963 = 3.506\ \Omega$$

The input phase voltage is

$$V_1 = \sqrt{(E_f + I_a R_1)^2 + (I_a X_{sq})^2}$$

$$= \sqrt{(229.5 + 8.2 \times 1.122)^2 + (8.2 \times 3.506)^2} = 240.5\ \text{V}$$

The line–to–line voltage $V_{1L-L} = \sqrt{3} \times 240.5 = 416.5$ V.

The power factor is

$$\cos\phi = \frac{E_f + I_a R_1}{V_1} = \frac{229.5 + 8.2 \times 1.122}{240.5} = 0.993 \approx 1.0$$

Numerical Example 5.2

For the coreless stator AFPM brushless motor described in *Numerical example 5.1* find the rotor moment of inertia, mechanical and electromagnetic time constants and axial magnetic attractive force between the backing steel discs of the twin rotor.

Solution

The following input data and results of calculation of *Numerical example 5.1* are necessary:

- input phase voltage $V_1 = 240.5$ V
- input frequency $f = 150$ Hz
- air gap magnetic flux density $B_{mg} = 0.607$ T
- Stator winding resistance per phase $R_1 = 1.122\ \Omega$

Hesai Exhibit 1032, page 196

- d-axis synchronous reactance $X_{sd} = 3.532\ \Omega$
- q-axis synchronous reactance $X_{sq} = 3.506\ \Omega$
- torque constant $k_T = 2.192$ Nm/A
- Electromagnetic torque $T_d = 19.97$ Nm
- speed $n = 3000$ rpm
- power factor $\cos\phi = 0.993$
- PM outer diameter $D_{out} = 0.22$ m
- PM inner diameter $D_{in} = 0.127$ m
- shaft diameter $D_{sh} = 2R_{sh} = 0.03$ m
- number of pole pairs $p = 3$
- pole width–to–pole pitch ratio $\alpha_i = 2/\pi$
- axial height of PM (one pole) $h_M = 6$ mm
- mass of twin rotor without shaft $m_r = 3.4$ kg
- mass of shaft $m_{sh} = 0.64$ kg
- specific mass density of PMs $\rho_{PM} = 7700$ kg/m^3
- specific mass density of mild steel $\rho_{Fe} = 7850$ kg/m^3

1. Rotor moment of inertia

The active surface area of PMs (one side) according to eqn (2.63) is

$$S_{PM} = \frac{2}{\pi}\frac{\pi}{4}(0.22^2 - 0.127^2) = 0.01614\ \text{m}^2$$

The mass of all PMs is

$$m_{PM} = 2 \times 7700 \times 0.01614 \times 0.006 = 1.49\ \text{kg}$$

The mass of backing steel discs is

$$m_{Fe} = m_r - m_{PM} = 3.4 - 1.49 = 1.91\ \text{kg}$$

The shaft moment of inertia is

$$J_{sh} = m_{sh}\frac{D_{sh}^2}{8} = 0.64\frac{0.03^2}{8} = 0.072 \times 10^{-3}\ \text{kgm}^2$$

The moment of inertia of PMs is

$$J_{PM} = m_{PM}\frac{D_{out}^2 + D_{in}^2}{8} = 1.49\frac{0.22^2 + 0.127^2}{8} = 0.012\ \text{kgm}^2$$

The moment of inertia of backing steel discs is

$$J_{Fe} = m_{Fe}\frac{D_{out}^2 + D_{sh}^2}{8} = 1.91\frac{0.22^2 + 0.03^2}{8} = 0.0118\ \text{kgm}^2$$

The resultant moment of inertia of the rotor is

$$J_r = J_{sh} + J_{PM} + J_{Fe} = 0.072 \times 10^{-3} + 0.012 + 0.0118 = 0.02386\ \text{kgm}^2$$

Hesai Exhibit 1032, page 197

2. Mechanical and electromagnetic time constants

Since the d-axis current $I_{ad} = 0$, the angle between the q axis and stator current $\psi = 0$. For the power factor $\cos\phi = 0.993$ the angle between stator current and terminal voltage $\phi = 6.78^{\circ}$. The load angle is

$$\delta = \phi - \psi = 6.78 - 0 = 6.78^{\circ}$$

At the first instant of starting the EMF $E_f = 0$. Assuming the load angle at starting is the same as for nominal operation, the stator current according to eqns (2.87), (2.88) and (2.89) is

$$I_{ashd} = \frac{240.5(3.506 \times 0.993 - 1.122 \times 0.118) - 0 \times 3.506}{3.532 \times 3.506 + 1.122^2} = 59.04 \text{ A}$$

$$I_{ashq} = \frac{240.5(1.122 \times 0.993 + 3.532 \times 0.118) - 0 \times 1.122}{3.532 \times 3.506 + 1.122^2} = 27 \text{ A}$$

$$I_{ash} = \sqrt{59.04^2 + 27^2} = 64.92 \text{ A}$$

where $\sin\phi = 0.118$ ($\cos\phi = 0.993$). The electromagnetic starting torque according to eqn (2.33) is

$$T_{dst} = k_T I_{ashq} = 2.192 \times 27.0 = 59.2 \text{ Nm}$$

The no load speed assuming linear torque-speed curve according to eqn (2.133) is

$$n_0 = \frac{3000}{1 - 19.97/59.2} = 4526.9 \text{ rpm} = 75.44 \text{ rev/s}$$

The mechanical time constant is

$$T_{mech} = J_r \frac{2\pi n_0}{T_{dst}} = 0.02386 \frac{2\pi 75.44}{59.2} = 0.191 \text{ s}$$

The d- and q-axis synchronous inductances are

$$L_{sd} = \frac{X_{sd}}{2\pi f} = 3.5322\pi 150 = 0.00375 \text{ H}$$

$$L_{sq} = \frac{X_{sq}}{2\pi f} = 3.5062\pi 150 = 0.00372 \text{ H}$$

The electromagnetic time constant of the stator winding is

Hesai Exhibit 1032, page 198

$$T_{elm} = \frac{L_{sd}}{R_1} = \frac{0.00375}{1.122} = 0.00334 \text{ s}$$

The mechanical–to–electromagnetic time constant ratio is

$$\frac{T_{mech}}{T_{elm}} = \frac{0.191}{0.00334} = 57.2$$

3. Axial attractive force between backing steel discs of the twin rotor

Assuming that the two twin backing steel discs are perfectly parallel, the axial magnetic attractive force between them can be found on the basis of eqn (5.39)

$$F_z = \frac{0.606^2}{2\mu_0} 0.01614 = 2365.5 \text{ N}$$

The magnetic pressure is

$$p_z = \frac{F_z}{S_{PM}} = \frac{2365.5}{0.01614} = 146\ 601.2 \text{ Pa} \approx 146.6 \text{ kPa}$$

The backing steel disc thickness is

$$d_{Fe} = \frac{m_{Fe}}{2\rho_{Fe}\pi(D_{out}^2 - D_{in}^2)/4}$$

$$= \frac{1.91}{2 \times 7850\pi(0.22^2 - 0.127^2)/4} = 0.0033 \text{ m} = 3.3 \text{ mm}$$

and outer diameter $D_{out} = 0.22$ m can provide adequate stiffness of the disc under the action of 146.6 kPa magnetic pressure in the axial direction.

Hesai Exhibit 1032, page 199

6

AFPM Machines Without Stator and Rotor Cores

6.1 Advantages and Disadvantages

With the availability of high energy magnets the stators and rotors of AFPM brushless machines can be fabricated without ferromagnetic cores [107, 150, P83, 225]. A completely coreless design reduces the mass and increases the efficiency of the machine as compared with a conventional design. Besides this, a coreless AFPM brushless machine does not produce any normal attractive force between the stator and rotor. It also does not produce torque pulsations at zero current state.

There is a limit to the increase of the electromagnetic torque that can be achieved by enlarging the machine diameter. Factors limiting the single disc design are listed in Section 2.1.6. A reasonable solution for larger torques are double or triple-disc machines.

The disc-type PM brushless machines without stator and rotor cores were first manufactured commercially in the late 1990s for servo mechanisms and industrial electromechanical drives [150], solar powered electrical vehicles [225] as well as micromotors for computer peripherals and vibration motors for mobile phones [93].

6.2 Topology and Construction

The *AFPM brushless machine without any ferromagnetic core* is shown in Fig. 6.1. The machine consists of a twin rotor (3) with rare earth PMs (2) and nonmagnetic supporting structure. The steel-free stator (armature) winding (1) is located between two identical parts of the rotor. The stator polyphase winding fixed to the frame (6) is assembled as "flower petals" (Fig. 3.16) [P83]. Multi-turn coils are arranged in overlapping layers around the shaft-axis of the machine. The whole winding is then embedded in a high mechanical integrity plastic or resin. Since the topology shown in Fig 6.1 does not use any ferromagnetic core with slots, the machine is free of cogging (detent) torque

Hesai Exhibit 1032, page 200